Article

Wind Turbine Wake Characterization with Nacelle-Mounted Wind Lidars for Analytical Wake Model Validation

Fernando Carbajo Fuertes [1], Corey D. Markfort [2,3] and Fernando Porté-Agel [1,*]

[1] Wind Engineering and Renewable Energy laboratory (WiRE)-École polytechnique fedérale de Lausanne (EPFL), Lausanne 1015, Switzerland; fernando.carbajo@epfl.ch
[2] IIHR-Hydroscience & Engineering, The University of Iowa, Iowa City, IA 52242, USA; corey-markfort@uiowa.edu
[3] Civil and Environmental Engineering, The University of Iowa, Iowa City, IA 52242, USA
[*] Correspondence: fernando.porte-agel@epfl.ch; Tel.: +41-(0)-21-693-61-38

check for updates

Abstract: This study presents the setup, methodology and results from a measurement campaign dedicated to the characterization of full-scale wind turbine wakes under different inflow conditions. The measurements have been obtained from two pulsed scanning Doppler lidars mounted on the nacelle of a 2.5 MW wind turbine. The first lidar is upstream oriented and dedicated to the characterization of the inflow with a variety of scanning patterns, while the second one is downstream oriented and performs horizontal planar scans of the wake. The calculated velocity deficit profiles exhibit self-similarity in the far wake region and they can be fitted accurately to Gaussian functions. This allows for the study of the growth rate of the wake width and the recovery of the wind speed, as well as the extent of the near-wake region. The results show that a higher incoming turbulence intensity enhances the entrainment and flow mixing in the wake region, resulting in a shorter near-wake length, a faster growth rate of the wake width and a faster recovery of the velocity deficit. The relationships obtained are compared to analytical models for wind turbine wakes and allow to correct the parameters prescribed until now, which were obtained from wind-tunnel measurements and large-eddy simulations (LES), with new, more accurate values directly derived from full-scale experiments.

Keywords: wind energy; atmospheric boundary layer; wind turbine wake; wind lidar; turbulence; wake modeling; field experiments

1. Introduction

The wind flow around the rotating blades of a wind turbine creates aerodynamic forces that result in a torque on the rotor axis, which ultimately generates electrical energy, and an axial thrust force, which pushes back the rotor. Following Newton's third law, these actions are compensated with reactions on the wind flow, altering its characteristics within a volume downstream of the wind turbine that is called the wake region [1]. The reaction force of the thrust creates an axial induction opposite to the air motion direction which reduces the kinetic energy of the flow, causing a reduction in velocity. The reaction torque, instead, creates a tangential induction which causes the flow to spin in the opposite sense of the rotation of the blades. Since the reaction aerodynamic forces have a dynamic nature and they generate important shear locally in the flow, they result as well in increased levels of turbulence. A wind turbine wake has two main negative effects on surrounding wind turbines within its area of influence. First, the kinetic energy deficit results in a decrease in energy production [2,3], and second, the higher turbulence levels result in higher fatigue loads and a potential life time reduction [4].

The correct understanding, characterization, and accurate modeling of wind turbine wakes is of utmost importance for accurate power prediction of wind farms [5,6] as well as layout optimization [7,8]. Wind turbine wake models may also play a key role in the control of wind farms [9,10].

Wind turbine wake models can be analytical [11], numerical [12], empirical, or a mixture of them [13]. In all cases the wake models need to be validated with experimental data. Wind tunnel experiments present some advantages for validation purposes (e.g., repeatability, flow control, wind turbine control, wind farm layout, etc.) [14–20] but it is very challenging to ensure complete flow similarity for scaled tests [21]. Ideally, the validation would include a comparison of model prediction under different conditions of the atmospheric boundary layer (ABL) with measurements of full scale wind turbine wakes. The measurement technique best suited to measurements of the wake is the wind lidar (Light Detection and Ranging), which is a remote sensing measurement technique based on the Doppler effect of reflected laser light from aerosol. A pulsed wind lidar, in particular, is able to measure wind speed with relatively high spatial and temporal resolutions (around 20 m and 10 Hz can be easily achieved with state-of-the-art systems under normal atmospheric conditions) up to distances of a few kilometers.

Comparing full-scale measurements of wind turbine wakes and model predictions is particularly challenging and presents a number of difficulties, especially given the limited amount of data available during the experiments. The discussion presented by Barthelmie et al. [22] is particularly interesting and relevant for this manuscript. They address the issues related to correctly establishing the free stream flow characteristics (i.e., horizontal wind speed, wind direction, nacelle orientation and yaw misalignment, turbulence intensity and atmospheric stability), to the accuracy of the site specific power curve and thrust coefficients, and to ensuring equivalent time averaging in models and measurements. These difficulties often arise from two important sources, which are the horizontal inhomogeneity and the non-stationarity of the atmospheric flow (i.e., the horizontal gradients and the natural fluctuations in the wind speed and direction in any period).

Recently, an increasing number of studies have investigated wind turbine wakes either via planar or volumetric scans with ground-based scanning lidars [23–31] using different scanning strategies and post-processing algorithms. Nevertheless, nacelle-based lidar experiments [32–36] have inherent advantages when measuring wakes. Some of these advantages are: the lidar always has the same alignment with the rotor, this alignment is independent from the wind direction, the errors due to the assumption of unidirectional average flow are smaller, and it can perform horizontal planar scans of the wake.

The objective of this study is to present an experimental setup and data post processing methodology for the characterization of single wind turbine wakes under different atmospheric conditions based on two nacelle-mounted lidars. The first lidar is upstream-looking and it is dedicated to the characterization of the inflow conditions in terms of average wind speed, turbulence intensity, yaw and vertical wind shear. The second lidar is downstream-looking and executes horizontal plan position indicator (PPI) scans of the wake. This allows accurate measurements of the velocity deficit in the wake and is ideal for the comparison with the predictions from wake models.

2. Methodology

This section describes the characteristics of the site where the tests were performed, as well as the meteorological tower, the wind turbine, the lidar setup, and the methodology used to analyze the data.

2.1. Test Site

The selected test site is located at the Kirkwood Community College campus, in the state of Iowa. The wind turbine studied is a 2.5 MW Liberty C96 model, manufactured by Clipper Windpower. It is equipped with a Supervisory Control And Data Acquisition (SCADA) system which continuously collects data at 10 min intervals about the wind turbine operation. The main characteristics of the wind turbine are detailed in Table 1.

Table 1. Wind turbine main characteristics.

Clipper Windpower-Liberty C96	
Rated power	2.5 MW (at 15 m/s)
Rotor diameter (D)	96 m
Tower height	80 m
Minimum rotor speed	9.5 rpm
Maximum rotor speed	15.5 rpm
Cut-in wind speed	4 m/s
Cut-off wind speed	25 m/s

Figure 1 shows the power coefficient of the wind turbine and the blade pitch angle imposed by the control system as function of the incoming wind speed as registered by the SCADA system. This information helps determining the range of usable wind speeds for the analysis of the wake. The power coefficient C_P is quasi-constant and close to a value of 0.37 for velocities between 5 and 10 m/s. This is the range of velocities where the wind turbine operates optimally and therefore the aerodynamic forces are most important. Once the wind velocity reaches 10 m/s the control system changes the pitch angle of the blades, reducing the aerodynamic efficiency of the rotor and effectively decreasing the thrust forces. We consider that the thrust coefficient C_T is close to constant within the same range of wind speeds, which is common in most wind turbines, and limit the study of the wake to this range. In the absence of manufacturer's data, and given the similarity in terms of thrust coefficient from commercial wind turbines, a value of $C_T = 0.82$ is estimated for the 5–10 m/s wind speed range.
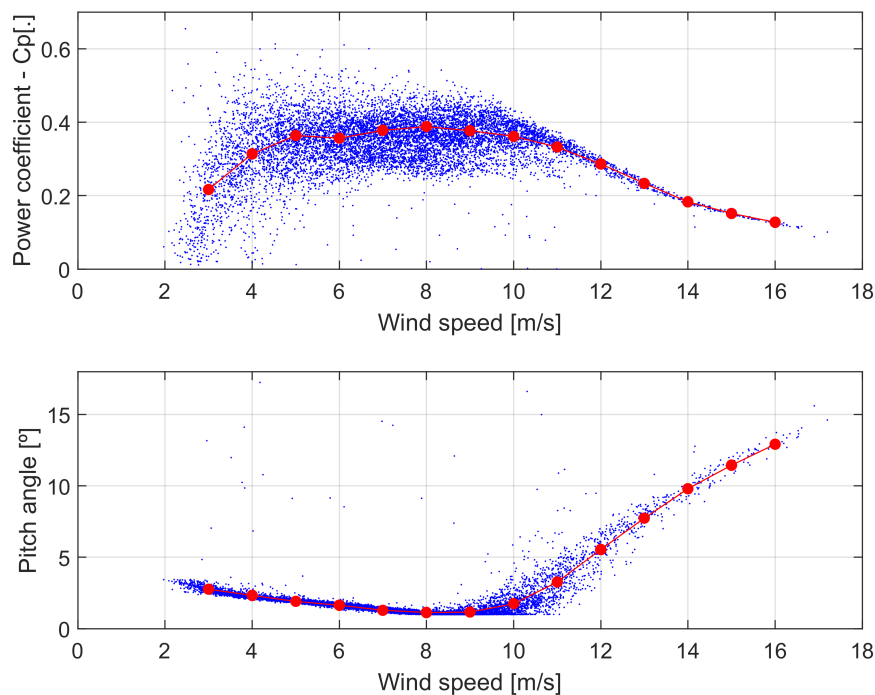

Figure 1. Power coefficient and blade pitch angle as a function of the wind speed for the 2.5 MW Liberty C96 wind turbine obtained from SCADA data. The 10 min values are shown in blue dots and binned averages in red. A quasi constant power coefficient is observed for wind speeds from 5 to 10 m/s.

Figure 2 shows a satellite image of the Kirkwood Community College campus and its surroundings with the location of the wind turbine and the meteorological tower. The predominant wind directions in the area are NW and SSE as shown in Figure 3. The wind turbine is situated at an elevation of 246 m and the surrounding terrain can be considered as rolling terrain. In an area of

3 km around the turbine the maximum elevation difference does not exceed 30 m and the terrain slope rarely exceeds 1%. The surface roughness, which plays a role in the ambient turbulence of the ABL, changes from higher roughness lengths associated to the suburban area of the city of Cedar Rapids (W to N directions) to lower values associated to agricultural fields (NE to SW directions). The campus is equipped with a 106 m tall meteorological tower situated at a distance of approximately 900 m from the wind turbine towards the SSW direction. The tower is equipped with sonic anemometers, cup anemometers and wind vanes—among other instruments—situated at heights of 10, 32, 80 and 106 m for the characterization of the ABL.

Figure 2. Location of the wind turbine and the meteorological tower inside Kirkwood's campus as well as the outskirts of Cedar Rapids. Map data: Google, Image NASA.

Figure 3 presents the wind rose for the last ten years obtained from measurements at the Eastern Iowa Airport, shown in the lower left corner of Figure 2. The airport is situated approximately 5 km to the SW of the test site. The wind presents two main directions: NW are affected by relatively high surface roughness of the suburban area of Cedar Rapids, while SSE are affected by the lower roughness of the agricultural fields.
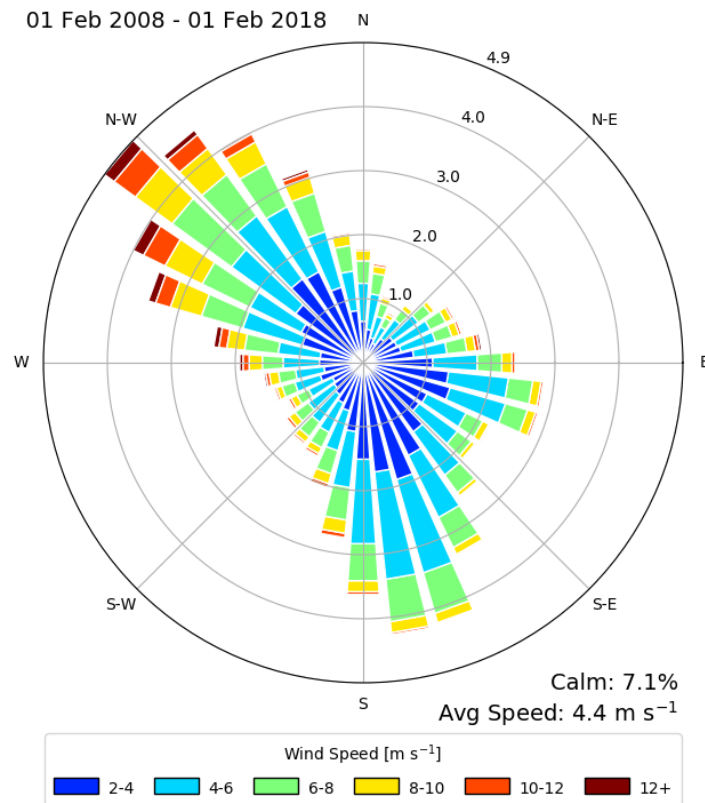
Figure 3. Wind rose measured at the Eastern Iowa Airport for 10 years, situated approximately 5 km to the SW of the wind turbine and visible in Figure 2. The wind presents two main directions: NW and SSE. Data obtained from Iowa State University, Iowa Environmental Mesonet. The length of the bars indicate frequency in percentage units.

2.2. Lidar Setup

The two lidar units used in the experiment are StreamLine models manufactured by Halo-Photonics. These instruments are infrared Doppler pulsed wind lidars which emit 1.5 μm wavelength pulses at a frequency of 10 kHz. They are scanning lidars, which means that the laser beam can be oriented towards any direction thanks to a steerable head. The units are able to provide measurements of the radial velocity with a resolution of 3.82 cm/s at intervals of 18 m along the laser beam direction or Line-of-Sight (LoS) and their measurement range extends from 63 m to more than 1000 m under most atmospheric conditions.

Both lidars are mounted on level platforms installed on the nacelle of the wind turbine. The first unit is an upstream-looking lidar dedicated to the characterization of the incoming flow conditions of the ABL and the second one is a downstream-looking lidar dedicated to the characterization of the wind turbine wake. A sketch of the lidar setup measurement configuration is presented in Figure 4. The forward-looking lidar laser beam is commonly blocked by the passage of the wind turbine blades and a quality check algorithm is implemented in order to filter out blocked measurements. Between 5 and 20% of the measurements are rejected under normal operating conditions, although this rarely compromises the analysis of the inflow data.
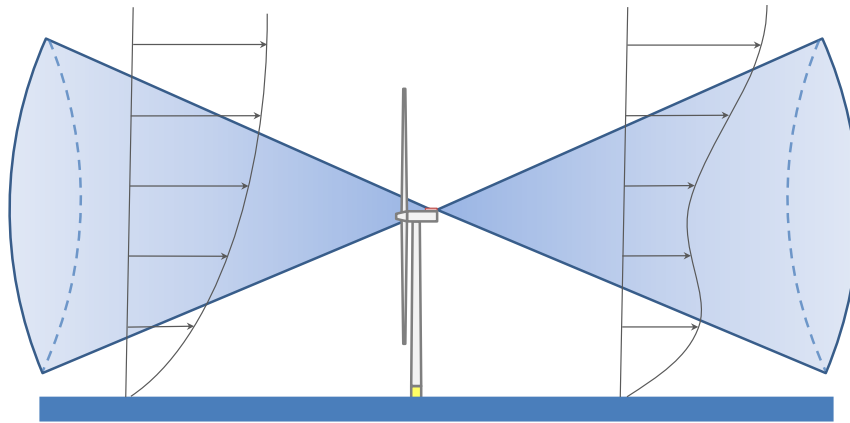
Figure 4. Sketch of the lidar setup with one lidar dedicated to the measurement of the incoming flow conditions and another one dedicated to the characterization of the wake.

2.3. Upstream Scanning

Both the inflow and the wake scans are grouped into synchronized periods of 30 min. The length of the periods is a compromise between the need for multiple samples in order to decrease the statistical error of the measurements and the requirement of stationarity of the flow. Each period of upstream scanning is divided into four successive scans that quantify different variables of the incoming flow. The calculations assume horizontally homogeneous flow in the region 250–600 m (2.6–6.25D) upstream of the rotor. Only measurements within this range are taken into consideration. Some of the measurements are redundant, such as the wind speed at hub height U_{hub}, yaw angle γ and longitudinal turbulence intensity TI_x, and they help to understand the degree of stationarity of the atmospheric conditions during the 30 min periods. The sub-indexes *ppi*, *rhi* and *st* indicate parameters obtained from Range Height Indicator (RHI), Plan Position Indicator (PPI) and staring-mode scans respectively.

An example of the characterization of the inflow conditions for the period between 22h30 and 23h00 (GMT-6) of 15 September 2017 is provided in the following subsections.

2.3.1. Yaw

The determination of the yaw angle γ_{ppi} and the wind speed at hub height $U_{hub,ppi}$ is done with upstream horizontal PPI scans of a $\pm60°$ range around the rotor axis direction. The scans are performed at an angular resolution of $4°$ and a measurement frequency of 3 Hz during 5 min. The yaw angle and the wind speed at hub height are determined by fitting a cosine function to the radial velocities as a function of the azimuth angle φ as detailed in the following equation:

$$Vr(\varphi) = U_{hub,ppi} \cos(\varphi - \gamma_{ppi}).$$

(1)

The azimuth angle is defined as the horizontal angle between the laser beam orientation and the downstream axis of the rotor. An example of the wind speed is provided in Figure 5 where one can see all the radial velocity measurements taken in the upstream range previously described and plotted against the azimuth angle, the cosine fit and the calculated yaw angle.
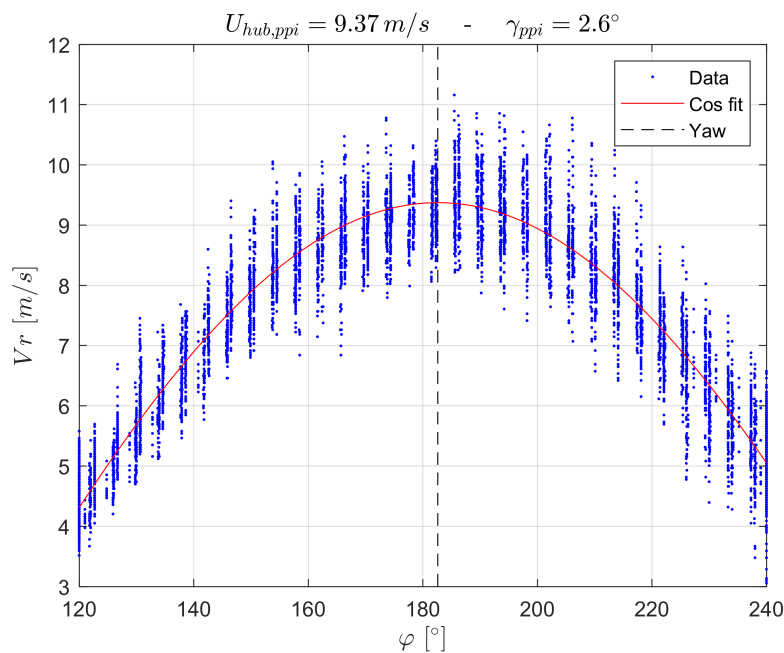
Figure 5. Example of the estimation of the yaw angle and the horizontal wind speed at hub height with plan position indicator (PPI) scans. Data corresponding to the period 22h30–22h35, 15 September 2017.

2.3.2. Vertical Profile of the Horizontal Velocity

The determination of the vertical profile of horizontal velocity is done with upstream vertical Range Height Indicator (RHI) scans aligned with the rotor axis direction of a $\pm 15°$ around the horizontal plane. The scans are performed with an angular resolution of $1°$ in the elevation angle θ and a frequency of 3 Hz during 5 min. The measurements of radial velocity are corrected with the elevation angle and the yaw angle previously quantified in Section 2.3.1 in order to obtain an estimation of the undisturbed horizontal velocity at different heights:

$$u_\infty(z) = Vr(z)/(\cos(\theta)\cos(\gamma_{ppi})) \,. \tag{2}$$

The measurements of the horizontal component of the wind velocity are divided into blocks of 10 m in the vertical direction, and the average $U_\infty(z)$ and standard deviation $\sigma_{u,rhi}(z)$ are calculated. From these vertical profiles it is possible to extract the values at hub height of the mean horizontal velocity $U_{hub,rhi}$ and the longitudinal turbulence intensity $TI_{x,rhi} = \sigma_{u,rhi}(z_{hub})/U_{hub,rhi}$. An example is provided in Figure 6. Figure 6a shows all the corrected horizontal wind speed measurements taken in the upstream range previously described and plotted against height, while Figure 6b shows the binned statistics for each block of 10 m in the vertical direction.
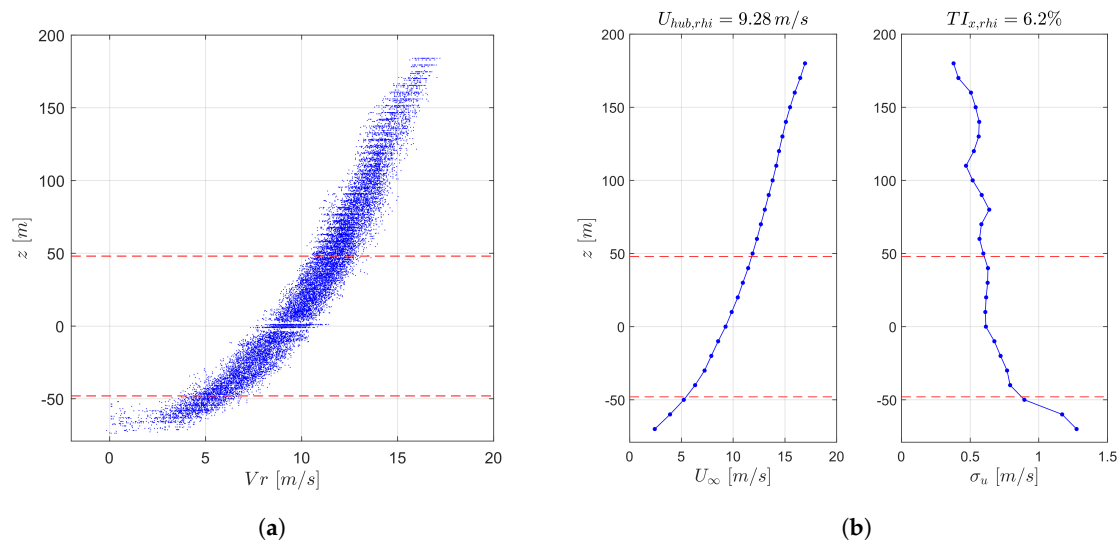
Figure 6. Example of the characterization of the vertical profile of horizontal velocity with range height indicator (RHI) scans. The red dashed lines indicate the upper and lower limits of the rotor. (**a**) All measurements; (**b**) Binned statistics. 22h35–22h40, 15 September 2017.

2.3.3. Turbulence Intensity

The determination of the longitudinal turbulence intensity $TI_{x,st}$ and a supplementary calculation of the wind speed at hub height $U_{hub,st}$ is done with a staring-mode scan aligned with the rotor axis direction for a duration of 10 min. Measurements are taken at a frequency of 1.5 Hz. Only the measurements of radial velocity in the mentioned upstream range are considered and their average and standard deviation calculated. The wind speed at hub height is corrected with the yaw angle previously calculated in Section 2.3.1:

$$U_{hub,st} = \overline{Vr}_{(\varphi=0°)} / \cos(\gamma_{ppi}). \tag{3}$$

The standard deviations of the longitudinal component of the wind speed and the radial velocity are equated:

$$\sigma_u = \sigma_{Vr(\varphi=0°)}, \tag{4}$$

and the longitudinal turbulence intensity is calculated as:

$$TI_{x,st} = \sigma_u / U_{hub,st}. \tag{5}$$

The transversal turbulence intensity calculation uses a horizontal staring-mode scan of the same duration at an angle of 90° with the rotor axis direction. The same relationship between the standard deviations of the longitudinal component of the wind speed and the radial velocity is used:

$$\sigma_v = \sigma_{Vr(\varphi=90°)}, \tag{6}$$

Additionally, the transversal turbulence intensity is calculated as:

$$TI_{y,st} = \sigma_v / U_{hub,st}. \tag{7}$$

A supplementary estimation of the yaw angle can be obtained by:

$$\gamma_{st} = \tan^{-1}\left(\overline{Vr}_{(\varphi=90°)} / U_{hub,st}\right) \tag{8}$$

The calculated values of the wind speed and longitudinal turbulence intensity for the period 22h40–22h50, 15 September 2017, are $U_{hub,st} = 9.12$ m/s and $TI_{x,st} = 5.7\%$. The values of the longitudinal turbulence intensity and yaw angle for the period 22h50–23h00 are $TI_{y,st} = 4.2\%$ and $\gamma_{st} = 2.17°$.

2.4. Downstream Scanning and Reconstruction of Planar Velocity Fields

The wake scanning consists of consecutive downstream horizontal PPI scans with a range of $\pm 20°$ around the rotor axis direction. The scans are performed at an angular resolution of $2°$ and a frequency of 2 Hz during 30 min.

The reconstruction of the longitudinal velocity fields in terms of its average and standard deviation follows these steps:

1. The average radial velocity $\overline{Vr}(\varphi, r)$ and its standard deviation $\sigma_{Vr}(\varphi, r)$ for all PPI scans are calculated at each point in space separated $2°$ in the azimuth φ and 18 m in the radial direction r, conforming a regular polar grid.

2. The average radial velocity is corrected with the calculated yaw angle γ_{ppi} in order to estimate the longitudinal velocity component:

$$\overline{u}(\varphi, r) = \overline{Vr}(\varphi, r) / \cos(\gamma_{ppi} - \varphi) . \tag{9}$$

3. The standard deviation of the streamwise velocity component and the radial velocity are assumed to be the same and are directly equated:

$$\sigma_u(\varphi, r) = \sigma_{Vr}(\varphi, r) . \tag{10}$$

4. The values in the polar grid are interpolated linearly into a Cartesian grid of 10 m resolution obtaining $\overline{u}(x, y)$ and $\sigma_u(x, y)$, more suitable to the post-processing of the data and the comparison with wake models.

An example of the average and standard deviation fields is provided in Figure 7, where it is possible to see the effect of the interpolation from polar coordinates to Cartesian. The interpolation from a polar grid with a resolution of $2°$ and 18 m into a Cartesian one with a resolution of 10 m means that the data will be slightly oversampled overall except closer to the rotor, where it will be slightly downsampled in the transversal direction. This should not affect the results obtained from the post-processing of the data. Although the turbulence fields of the wind turbine wake are not used in this study, the authors consider illustrative to show it as proof of the potential of the simple reconstruction technique used from PPI scans.
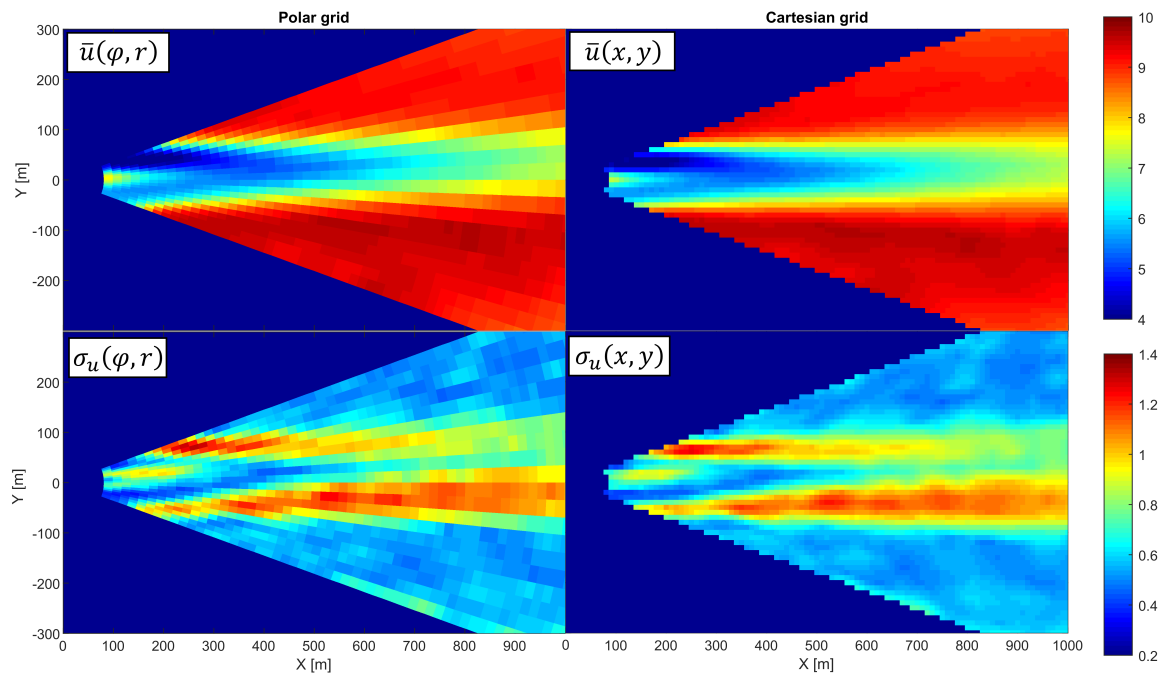
Figure 7. Example of the average and standard deviation of the wake in polar and Cartesian coordinates. 22h30–23h00, 15 September 2017. Units in m/s.

2.5. Wake Analysis

The analysis of the measurement of the wake of the wind turbine will vary depending on the objective of the study (e.g., wake meandering, yaw and skew angles, near/far wake determination, etc.). In this case the objective is the comparison with the predictions of the analytical model by Bastankhah and Porté-Agel in [11], who assumed Gaussian velocity deficit profiles in the far wake region and used mass and momentum conservation to link the growth rate of the wake and the recovery of the velocity deficit for different inflow conditions.

The local velocity deficit is defined as the difference between the local wind speed and the undisturbed wind speed at hub height:

$$\Delta \overline{u}(x,y) = U_{hub} - \overline{u}(x,y)\,. \tag{11}$$

The far wake of the wind turbine is defined as the region of the wake that exhibits self-similar velocity deficit transversal profiles, which are well approximated by a Gaussian function of the form:

$$\Delta \overline{u}(x,y) = C(x)e^{-\frac{(y-y_c(x))^2}{2\sigma_y(x)^2}}\,, \tag{12}$$

where C is the amplitude in m/s and corresponds to the velocity deficit along the centerline, y_c corresponds to the deviation of the center of the wake in meters from the longitudinal rotor axis and, finally, σ_y is the standard deviation in meters and corresponds to the wake width. In order to avoid contamination from data outside the area of interest, such as horizontal inhomogeneities of the free stream wind flow, the Gaussian fit to measured data uses a weighted nonlinear least squares regression. The weighting function is the resulting Gaussian function, but 50% wider. The goodness of the fit has been estimated by calculating the correlation ρ between measured and Gaussian fitted velocity profiles. It gives an indication of the beginning of the far wake region, or, conversely, the length of the near wake ℓ_{nw}. A value of $\rho = 0.99$ has been selected in [37] as the threshold to determine this distance.

An example of the analysis of a wind turbine wake is presented in Figure 8. In Figure 8a it is possible to see the velocity deficit vectors measured and the fitted Gaussian functions. It is noticeable the characteristic bimodal velocity deficit profile in the near wake, where a Gaussian function is not a good representation. In contrast, in the far wake the velocity deficit profile is self similar and shows an almost perfect fit to a Gaussian function. Figure 8b shows the longitudinal evolution of the Gaussian parameters of the fit. The first plot from the top shows the correlation coefficient between the measured velocity deficit and the Gaussian fit, together with the threshold $\rho = 0.99$ that indicates the beginning of the far wake [37]. In the case depicted it occurs at a distance of 3.9D from the rotor. The second plot shows the growth of the wake width in the longitudinal direction. Several wake models assume a linear expansion of the wake and it is possible to observe that it is a good assumption for the far wake region. The figure shows the coefficients of the linear fit in the form:

$$\sigma_y(x) = \left(k^* \frac{x}{D} + \varepsilon\right) D,\tag{13}$$

where D is the rotor diameter, k^* is the longitudinal growth rate of the wake width and ε is the wake width at the rotor plane.

The third plot of Figure 8b shows the velocity deficit along the centerline C and its decrease in the longitudinal direction, corresponding to the recovery of the wake velocity. Based on conservation of mass and momentum, this parameter has been linked to the wake width in the far wake by the following relationship [11]:

$$\frac{C(x)}{U_{hub}} = 1 - \sqrt{1 - \frac{C_T}{8(\sigma_y(x)/D)^2}}.\tag{14}$$

The plot also shows in a continuous red line the prediction of the C parameter by the analytical model, which shows good agreement for the far wake using the calculated wake expansion from the previous quadrant. It is also possible to observe that the prediction deviates substantially from the measured values when the Gaussian profile is not a good representation of the velocity deficit profile ($\rho < 0.99$). Finally, the last plot shows the deviation of the center of the Gaussian profile from the axis of rotation. The deviation follows a linear trend for the far wake as well and it is possible to calculate the skew angle of the wake by:

$$\chi = \tan^{-1}(\partial y_c / \partial x),\tag{15}$$

which, in the case presented, is 1.3°. This parameter could be useful to study the relationship between the yaw angle and the skew angle.

The analysis procedure described above is applied to all the 30 min periods in which the experiment has been divided and results are presented in Section 3.
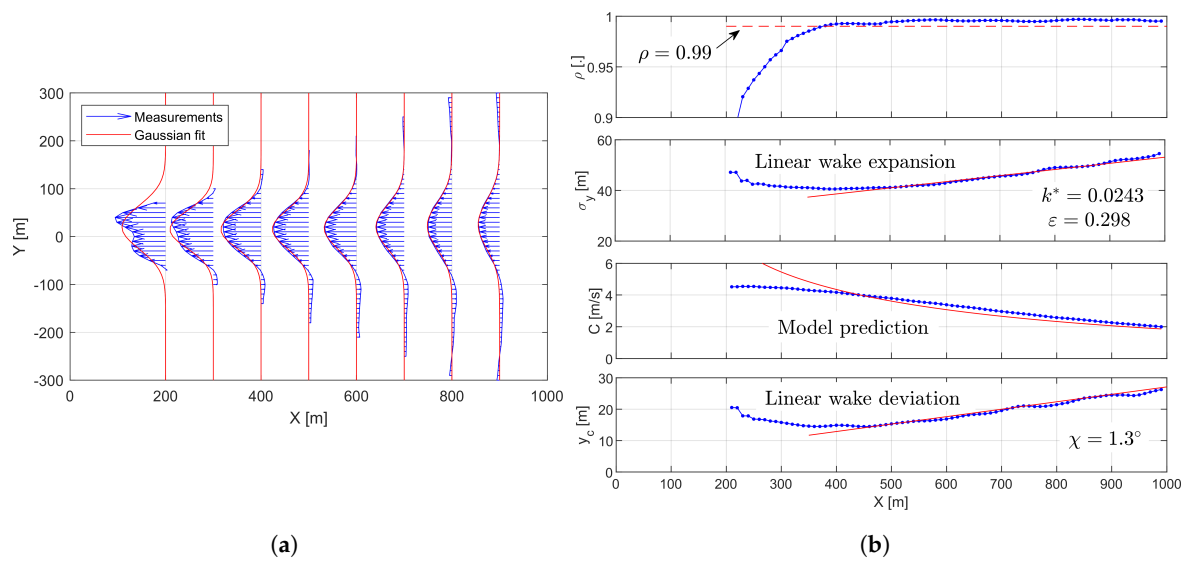
Figure 8. Example of the analysis of the wake of the wind turbine. (**a**) Velocity deficit and Gaussian fits; (**b**) Downstream evolution of the fit parameters. 22h30–23h00, 15 September 2017.

3. Results

This section describes the first measurements used for the analysis of the wake of the wind turbine as well as the conditions which entail a removal of those periods which are not suitable. The aggregated results are then presented and compared to data used to further validate and calibrate the analytical model discussed in Section 2.5.

The experiment data consists of a series of 30 min periods obtained between 20 August and 16 October 2017. One 30 min period is obtained every two hours for a total number of approximately 700. The inflow conditions for each period have been thoroughly studied in order to filter out those not suitable for the analysis of the wake. Criteria that were used to filter out measurement periods include (although are not limited to):

- Down times of the wind turbine.
- Wind speed outside the 5–10 m/s range.
- Low signal-to-noise ratio of the lidar measurements due to precipitation.
- Non-stationary undisturbed wind speed at hub height (comparison of $U_{hub,st}$, $U_{hub,ppi}$, $U_{hub,rhi}$).
- Non-stationary undisturbed wind direction at hub height (comparison of γ_{st}, γ_{ppi}).
- Non-stationary undisturbed turbulence intensity at hub height (comparison of $TI_{x,st}$, $TI_{x,rhi}$).
- Horizontal inhomogeneity of the wind speed in the surroundings of the wind turbine (this horizontal inhomogeneity can be easily observed when reconstructing the average of the longitudinal velocity field $\bar{u}(x,y)$ and observing the regions not affected by the wake. It can be seen that the case presented in Figure 7 shows a horizontally homogeneous flow outside the area of influence of the wake).
- Changing orientation of the rotor by the control system of the wind turbine.
- Measured yaw angles above $\pm 10°$.
- Disagreements among the inflow measured by the nacelle-mounted lidar, the data from the meteorological tower, and the SCADA data.

From all the collected data, only 44 periods have been selected as suitable for analysis, which yields a validity rate of around 6%. Three of the selected cases are shown for illustrative purposes in Figure 9. They are ordered in increasing inflow turbulence intensity at hub height from left to right. The top quadrants present the adimensional velocity deficit in the horizontal plane at hub height and it is

observed that the wind speed recovery occurs significantly faster for higher turbulence conditions. It is also observed that lower turbulence conditions retard the occurrence of a self-similar Gaussian velocity deficit profile, indicating there is a significantly longer near wake region. The bottom quadrants present the longitudinal turbulence intensity in the horizontal plane at hub height. It is observed that the background turbulence intensity levels in those areas not affected by the wind turbine wake as well as the turbulence generated by the shear, which is greatest in the mixing layers at the edge of the wake. The values of the incoming turbulence intensity, wake growth rate, wake width at the origin, and length of the near wake for these three cases are highlighted in Figures 10–12.
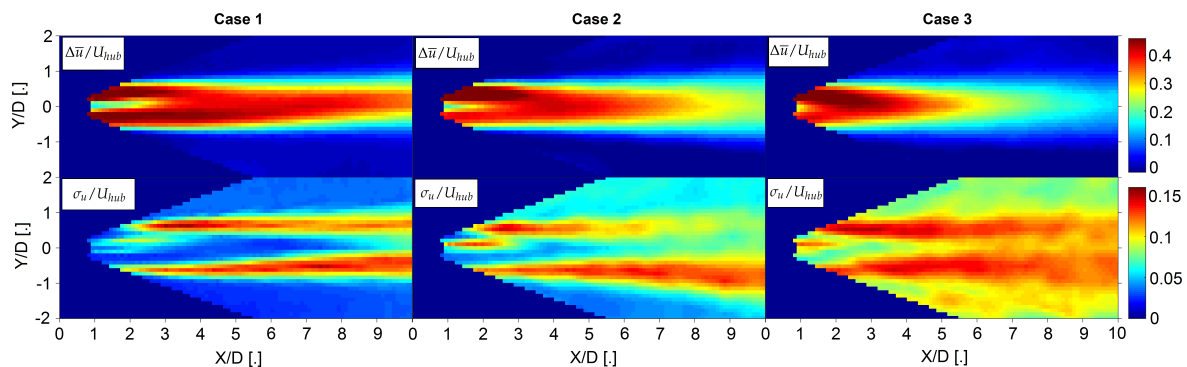

Figure 9. Example of three cases of wakes for increasing different longitudinal turbulence intensity conditions at hub height (Case 1–2.2%; Case 2–4.6%; Case 3–9.9%). The top quadrants present the adimensional velocity deficit while the bottom quadrants present the longitudinal turbulence intensity in the horizontal plane at hub height. These three example cases are further referenced in Figures 10–12.

The relationship found between the wake width growth rate k^* and the longitudinal turbulence intensity TI_x is presented in Figure 10. The data from the full scale field experiment (blue stars) as well as data from validated LES simulations (black squares) and wind tunnel experiment (black circle), presented in [11], agree well, taking into account the significant variability of the data. The data show clearly that the rate of growth of the wake width increases with the turbulence intensity. The growth of the wake is linked to the velocity recovery by mass and momentum conservation as already discussed. This implies a faster recovery of the velocity deficit for higher background turbulence since turbulence enhances flow mixing and the transfer of momentum from the undisturbed flow region into the wake. The linear fit to the full-scale field data is presented as a dashed red line in Figure 10, and it can be expressed as:

$$k^* = 0.35 \, TI_x . \tag{16}$$

The linear relationship of Equation (16) is similar to the one used in [38] by fitting a straight line to the data presented in [11], $k^* = 0.383 \, TI_x + 0.0037$ (presented as a dashed black line in Figure 10). When using these relationships, it is important to take into account the variability of the data, which indicates that it is not uncommon to find wake growths that differ by a factor of two or three for very similar conditions of longitudinal turbulence intensity. This suggests that further experiments should be addressed to understand the role of other variables that could also play an important role on the development of the wind turbine wake.

One particularly interesting effect to study is the occurrence of different wake growths in the vertical and horizontal directions, which makes the velocity deficit profiles not self-similar in the radial direction, leading to an elliptical profile instead of a circular one. Only considering the horizontal growth rate violates mass and momentum conservation and could be a reason for the variability of the results. Volumetric downstream scans with a similar setup have been performed during the same dates to further study this fact and preliminary analysis proves the occurrence of non circular velocity deficit profiles under certain atmospheric conditions. A more complete analysis can be provided in the future.
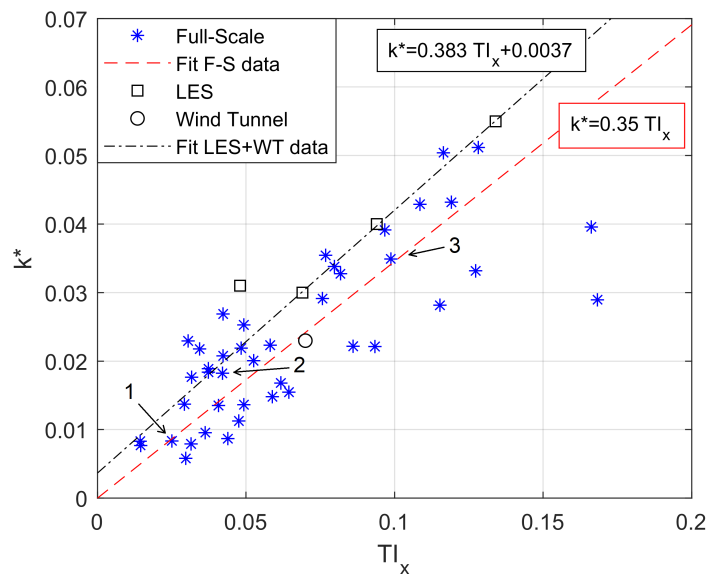
Figure 10. Relationship between wake growth k^* and longitudinal turbulence intensity TI_x. In blue all the data collected during the experiment, in dashed red the linear fit to the full-scale field data presented in Equation (16). In black the data obtained from [11] and the linear fit used in [38]. Numbers 1 to 3 indicate the cases presented in Figure 9.

The relationship between the growth rate of the wake and the wake width at the rotor plane ε is presented in Figure 11. ϵ is not physical, but rather a theoretical parameter, which indicates the hypothetical wake width at the rotor plane when considering a Gaussian wake from its origin (i.e., no existence of a near wake region). The correlation is negative, which means that for a higher growth rate, the width at the rotor plane is smaller. The figure presents the data obtained during this experiment (blue stars) together with its linear fit, which allows for the calculation of the wake width at the origin for a particular wake growth rate is presented as a dashed red line:

$$\epsilon = -1.91k^* + 0.34 \ . \tag{17}$$

The agreement between the full-scale field data and the data from the validated LES simulations (black squares) is good, but it is poor for the wind tunnel measurements (black circle).

Finally, the relationship between the length of the near wake ℓ_{nw} and the longitudinal turbulence intensity is presented in Figure 12. The setup used, and the range of the downstream PPI scans (see Section 2.4) does not allow for scans of the full width of the wake for shorter distances than approximately 200 m and, therefore, shorter near wake lengths are not included in the analysis. This is represented by the gray shaded area at the bottom of the figure. Similarly to the effect of the growth rate, a higher inflow turbulence intensity enhances flow mixing and this helps the wake reaching a self-similar state in a shorter distance. The length of the near wake reaches long distances, higher than six diameters in some cases, for particularly low turbulence flow. It can be observed that in this range of low turbulence intensities, the variability of the data becomes also greater.

A semi-analytical expression for the length of the near wake of a wind turbine under yaw conditions is presented in Bastankhah and Porté-Agel [19]. The corresponding relationship for zero or negligible yaw angles is:

$$\frac{\ell_{nw}}{D} = \frac{1 + \sqrt{1 - C_T}}{\sqrt{2}(\alpha \, TI_x + \beta \, (1 - \sqrt{1 - C_T}))} \ , \tag{18}$$

where β is a parameter obtained from analogy with jet flows and has a value of 0.154 and α is obtained from experimental data. The value of $\alpha = 2.32$ prescribed in [19] was obtained from wind-tunnel experiments. The expression for the length of the near wake using this value is represented in Figure 12 as a dashed

black line. A value of $\alpha = 3.6$ provides a better fit to the full scale experimental data, as shown by the red dashed line in Figure 12. It should be noted that the experimental data used in order to obtain the value of 3.6 is more exhaustive in terms of range of turbulence intensities covered and number of independent data points obtained.
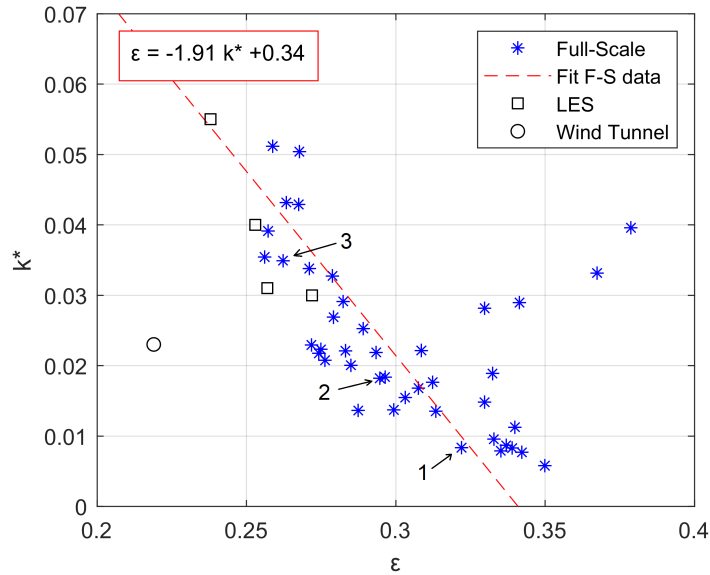

Figure 11. Relationship between wake growth k^* and wake width at the rotor ε. In blue all the data collected during the experiment, in dashed red the linear fit to the full-scale field data presented in Equation (17). In black the data obtained from [11]. Labels numbered 1 to 3 indicate the cases presented in Figure 9.
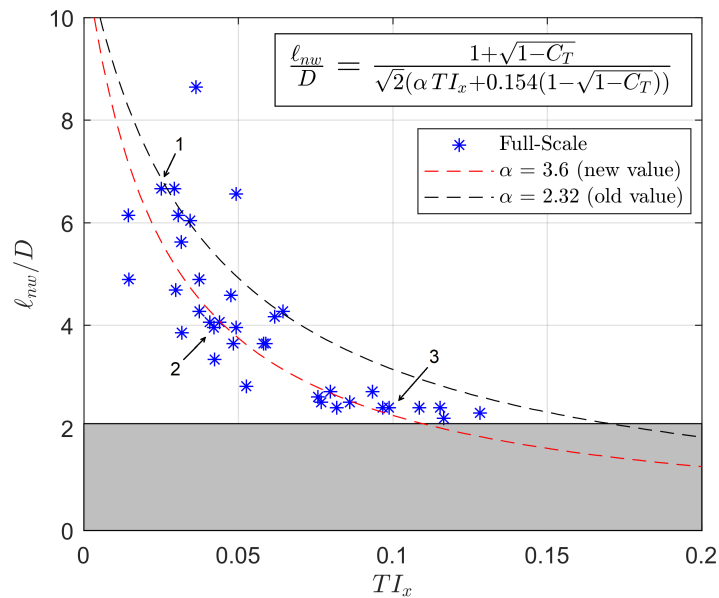

Figure 12. Relationship between near wake length ℓ_{nw} and longitudinal turbulence intensity TI_x. In blue all the data collected during the experiment, in dashed black Equation (18) for the estimation of the near wake length with the value of $\alpha = 2.32$ prescribed in [19] and in dashed red the same equation with the value of $\alpha = 3.6$ that provides a better fit to the full-scale field data. The grey rectangle at the bottom indicates the lowest bound for a possible calculation of the near wake length with the presented setup and analysis. Numbers 1 to 3 indicate the cases presented in Figure 9.

4. Conclusions

The study demonstrates that a measurement setup based on two nacelle-mounted lidars can be used to measure different characteristics of the incoming flow via RHI, PPI and staring-mode scans, while at the same time perform planar scans of the wake. The upstream oriented lidar data were processed with simple algorithms to calculate the vertical profile of horizontal velocity, the yaw angle of the incoming flow, and the longitudinal and transversal turbulence intensities. The downstream oriented lidar data were aggregated statistically and used to reconstruct the longitudinal velocity field in terms of its average and standard deviation. The velocity deficit profiles were fitted to Gaussian functions and provide information about the wake width and the velocity deficit along the center line at different longitudinal distances.

With the calculated inflow and wake parameters described above, it is possible to study the relationships between wake growth rate, wake width at the rotor plane, length of the near wake, and longitudinal turbulence intensity. A higher incoming turbulence increases mixing and the transfer of momentum from the regions outside the wake into it, reduces the length of the near wake, and increases the velocity recovery. A higher wake growth rate, in turn, implies a smaller wake width at the rotor plane. Different relationships have been established for these relationships.

The presented data have been compared to the predictions of the analytical wake model based on Gaussian velocity profiles and mass and momentum conservation developed by Bastankhah and Porté-Agel [11,19]. It has been found that the model predicts the wake expansion and velocity deficit well, as well as the length of the near wake region. The empirical parameters prescribed in the original model have been updated with the field experiment data.

This study can be extended to use volumetric measurements of the wake and using a similar methodology, in order to understand the implications in the development of the far wake under certain atmospheric conditions when the velocity deficit profile is not self-similar in the radial direction (i.e., not circular).

Author Contributions: This study was done as a part of Fernando Carbajo Fuertes doctoral studies supervised by Fernando Porté-Agel, and with the full support and collaboration from Corey D. Markfort.

Conflicts of Interest: The authors declare no conflict of interest. The founding sponsors had no role in the design of the study; in the collection, analysis, or interpretation of data; in the writing of the manuscript, and in the decision to publish the results.

Abbreviations

The following abbreviations are used in this manuscript:

ABL	Atmospheric Boundary Layer
LES	Large Eddy Simulation
LiDAR	Light Detection And Ranging
LoS	Line-of-Sight
RHI	Range Height Indicator
PPI	Plan Position Indicator
SCADA	Supervisory Control And Data Acquisition

References

1. Vermeer, L.; Sørensen, J.; Crespo, A. Wind turbine wake aerodynamics. *Prog. Aerosp. Sci.* **2003**, *39*, 467–510. [CrossRef]
2. Barthelmie, R.J.; Pryor, S.C.; Frandsen, S.T.; Hansen, K.S.; Schepers, J.G.; Rados, K.; Schlez, W.; Neubert, A.; Jensen, L.E.; Neckelmann, S. Quantifying the impact of wind turbine wakes on power output at offshore wind farms. *J. Atmos. Ocean. Technol.* **2010**, *27*, 1302–1317. [CrossRef]
3. Hansen, K.S.; Barthelmie, R.J.; Jensen, L.E.; Sommer, A. The impact of turbulence intensity and atmospheric stability on power deficits due to wind turbine wakes at Horns Rev wind farm. *Wind Energy* **2012**, *15*, 183–196. [CrossRef]
4. Thomsen, K.; Sørensen, P. Fatigue loads for wind turbines operating in wakes. *J. Wind Eng. Ind. Aerodyn.* **1999**, *80*, 121–136. [CrossRef]
5. Markfort, C.D.; Zhang, W.; Porté-Agel, F. Turbulent flow and scalar transport through and over aligned and staggered wind farms. *J. Turbul.* **2012**, *13*, N33. [CrossRef]
6. St. Martin, C.M.; Lundquist, J.K.; Clifton, A.; Poulos, G.S.; Schreck, S.J. Wind turbine power production and annual energy production depend on atmospheric stability and turbulence. *Wind Energy Sci. Discuss.* **2016**, 1–37.
7. Herbert-Acero, J.; Probst, O.; Réthoré, P.E.; Larsen, G.; Castillo-Villar, K. A Review of Methodological Approaches for the Design and Optimization of Wind Farms. *Energies* **2014**, *7*, 6930–7016. [CrossRef]
8. Gebraad, P.; Thomas, J.J.; Ning, A.; Fleming, P.; Dykes, K. Maximization of the annual energy production of wind power plants by optimization of layout and yaw-based wake control. *Wind Energy* **2017**, *20*, 97–107. [CrossRef]
9. Torben Knudsen, T.B.; Automation, M.S. Survey of wind farm control—Power and fatigue optimization. *Wind Energy* **2015**, *18*, 1333–1351. [CrossRef]
10. Chehouri, A.; Younes, R.; Ilinca, A.; Perron, J. Review of performance optimization techniques applied to wind turbines. *Appl. Energy* **2015**, *142*, 361–388. [CrossRef]
11. Bastankhah, M.; Porté-Agel, F. A new analytical model for wind-turbine wakes. *Renew. Energy* **2014**, *70*, 116–123. [CrossRef]
12. Sørensen, J.N.; Shen, W.Z. Numerical Modeling of Wind Turbine Wakes. *J. Fluid. Eng.* **2002**, *124*, 393. [CrossRef]
13. Crespo, A.; Hernández, J.; Frandsen, S. Survey of modelling methods for wind turbine wakes and wind farms. *Wind Energy* **1999**, *2*, 1–24. [CrossRef]
14. Chamorro, L.P.; Porté-Agel, F. A wind-tunnel investigation of wind-turbine wakes: Boundary-Layer turbulence effects. *Bound. Layer Meteorol.* **2009**, *132*, 129–149. [CrossRef]
15. Chamorro, L.P.; Porté-Agel, F. Turbulent flow inside and above awind farm: A wind-tunnel study. *Energies* **2011**, *4*, 1916–1936. [CrossRef]
16. Zhang, W.; Markfort, C.D.; Porté-Agel, F. Wind-Turbine Wakes in a Convective Boundary Layer: A Wind-Tunnel Study. *Bound. Layer Meteorol.* **2013**, *146*, 161–179. [CrossRef]
17. Lignarolo, L.E.; Ragni, D.; Krishnaswami, C.; Chen, Q.; Simão Ferreira, C.J.; van Bussel, G.J. Experimental analysis of the wake of a horizontal-axis wind-turbine model. *Renew. Energy* **2014**, *70*, 31–46. [CrossRef]
18. Iungo, G.V. Experimental characterization of wind turbine wakes: Wind tunnel tests and wind LiDAR measurements. *J. Wind Eng. Ind. Aerodyn.* **2016**, *149*, 35–39. [CrossRef]
19. Bastankhah, M.; Porté-Agel, F. Experimental and theoretical study of wind turbine wakes in yawed conditions. *J. Fluid Mech.* **2016**, *806*, 506–541. [CrossRef]
20. Bastankhah, M.; Porte-Agel, F. Wind tunnel study of the wind turbine interaction with a boundary-layer flow: Upwind region, turbine performance, and wake region. *Phys. Fluids* **2017**, *29*, 065105. [CrossRef]
21. Miller, M.A.; Kiefer, J.; Westergaard, C.; Hultmark, M. Model Wind Turbines Tested at Full-Scale Similarity. In *Journal of Physics: Conference Series*; IOP Publishing: Bristol, UK, 2016; Volume 753.
22. Barthelmie, R.J.; Hansen, K.; Frandsen, S.T.; Rathmann, O.; Schepers, J.G.; Schlez, W.; Phillips, J.; Rados, K.; Zervos, A.; Politis, E.S.; et al. Modelling and measuring flow and wind turbine wakes in large wind farms offshore. *Wind Energy* **2009**, *12*, 431–444. [CrossRef]

23. Käsler, Y.; Rahm, S.; Simmet, R.; Kühn, M. Wake measurements of a multi-MW wind turbine with coherent long-range pulsed doppler wind lidar. *J. Atmos. Ocean. Technol.* **2010**, *27*, 1529–1532. [CrossRef]

24. Iungo, G.V.; Wu, Y.T.; Porté-Agel, F. Field measurements of wind turbine wakes with lidars. *J. Atmos. Ocean. Technol.* **2013**, *30*, 274–287. [CrossRef]

25. Smalikho, I.N.; Banakh, V.A.; Pichugina, Y.L.; Brewer, W.A.; Banta, R.M.; Lundquist, J.K.; Kelley, N.D. Lidar investigation of atmosphere effect on a wind turbine wake. *J. Atmos. Ocean. Technol.* **2013**, *30*, 2554–2570. [CrossRef]

26. Iungo, G.V.; Porté-Agel, F. Volumetric lidar scanning of wind turbine wakes under convective and neutral atmospheric stability regimes. *J. Atmos. Ocean. Technol.* **2014**, *31*, 2035–2048. [CrossRef]

27. Banta, R.M.; Pichugina, Y.L.; Brewer, W.A.; Lundquist, J.K.; Kelley, N.D.; Sandberg, S.P.; Alvarez, R.J.; Hardesty, R.M.; Weickmann, A.M. 3D volumetric analysis of wind turbine wake properties in the atmosphere using high-resolution Doppler lidar. *J. Atmos. Ocean. Technol.* **2015**, *32*, 904–914. [CrossRef]

28. Aitken, M.L.; Banta, R.M.; Pichugina, Y.L.; Lundquist, J.K. Quantifying Wind Turbine Wake Characteristics from Scanning Remote Sensor Data. *J. Atmos. Ocean. Technol.* **2014**, *31*, 765–787. [CrossRef]

29. Doubrawa, P.; Barthelmie, R.; Wang, H.; Pryor, S.; Churchfield, M. Wind Turbine Wake Characterization from Temporally Disjunct 3-D Measurements. *Remote Sens.* **2016**, *8*, 939. [CrossRef]

30. El-Asha, S.; Zhan, L.; Iungo, G.V. Quantification of power losses due to wind turbine wake interactions through SCADA, meteorological and wind LiDAR data. *Wind Energy* **2017**, *20*, 1823–1839. [CrossRef]

31. Bodini, N.; Zardi, D.; Lundquist, J.K. Three-dimensional structure of wind turbine wakes as measured by scanning lidar. *Atmos. Meas. Tech.* **2017**, *10*, 2881–2896. [CrossRef]

32. Trujillo, J.; Bingöl, F.; Larsen, G.; Mann, J.; Kühn, M. Light detection and ranging measurements of wake dynamics. Part II: two-dimensional scanning. *Wind Energy* **2011**, *14*, 61–75. [CrossRef]

33. Aitken, M.L.; Lundquist, J.K. Utility-scale wind turbine wake characterization using nacelle-based long-range scanning lidar. *J. Atmos. Ocean. Technol.* **2014**, *31*, 1529–1539. [CrossRef]

34. Machefaux, E.; Larsen, G.C.; Troldborg, N.; Gaunaa, M.; Rettenmeier, A. Empirical modeling of single-wake advection and expansion using full-scale pulsed lidar-based measurements. *Wind Energy* **2015**, *18*, 2085–2103. [CrossRef]

35. Machefaux, E.; Larsen, G.C.; Koblitz, T.; Troldborg, N.; Kelly, M.C.; Chougule, A.; Hansen, K.S.; Rodrigo, J.S. An experimental and numerical study of the atmospheric stability impact on wind turbine wakes. *Wind Energy* **2016**, *19*, 1785–1805. [CrossRef]

36. Herges, T.G.; Maniaci, D.C.; Naughton, B.T.; Mikkelsen, T.; Sjöholm, M. High resolution wind turbine wake measurements with a scanning lidar. *J. Phys. Conf. Ser.* **2017**, *854*, 012021. [CrossRef]

37. Sorensen, J.N.; Mikkelsen, R.F.; Henningson, D.S.; Ivanell, S.; Sarmast, S.; Andersen, S.J. Simulation of wind turbine wakes using the actuator line technique. *Philos. Trans. R. Soc. A Math. Phys. Eng. Sci.* **2015**, *373*, 20140071. [CrossRef] [PubMed]

38. Niayifar, A.; Porté-Agel, F. Analytical modeling of wind farms: A new approach for power prediction. *Energies* **2016**, *9*, 741. [CrossRef]